# Nanotextured Silica Surfaces with Robust Superhydrophobicity and Omnidirectional Broadband Supertransmissivity

Kyoo-Chul Park,[†,∥] Hyungryul J. Choi,[†,∥] Chih-Hao Chang,[†,‡] Robert E. Cohen,[§] Gareth H. McKinley,[†,*] and George Barbastathis[†,⊥,*]

[†]Department of Mechanical Engineering, Massachusetts Institute of Technology, Cambridge, Massachusetts 02139, United States, [‡]Department of Mechanical & Aerospace Engineering, North Carolina State University, Raleigh, North Carolina 27695, United States, [§]Department of Chemical Engineering, Massachusetts Institute of Technology, Cambridge, Massachusetts 02139, United States, and [⊥]Singapore-MIT Alliance for Research and Technology (SMART) Centre, Singapore. [∥]These authors contributed equally to this work.

Natural biological surfaces have evolved to optimize their physico-chemical properties and structures at the micro/nanoscale for a wide variety of functions, ranging from wettability to optical properties.[1−3] Microscopic studies of the textured surfaces commonly encountered on living organisms, such as lotus leaves, desert beetles, and moth eyes, have revealed complementary roles of material properties and texture on the surface functionalities that have been developed during adaptation to different environments.[4−8] These studies have in turn inspired biomimetic surfaces emulating the self-cleaning,[9−13] water harvesting,[6] and antireflective[14−18] capabilities of functional surfaces found in nature. It has also been recognized recently that many natural surfaces are not optimized solely for their responsiveness to a single functional requirement; nature is an excellent architect for designing and optimizing surfaces that fulfill multiple purposes.[19]

Multifunctionality is also critical for practical engineering applications such as energy harvesting and operation of optical instrumentation in extreme climates or humid conditions where the wetting, reflectivity, and other surface properties must satisfy optimally multiple design characteristics in order to fulfill system requirements.[20,21] For example, the collecting efficiency of a photovoltaic solar cell is highly influenced by both surface dust contamination and Fresnel reflection losses over a broad range of wavelengths and incident angles.[15,20,21] The operational efficiency and longevity would benefit from both self-cleaning and antireflection surface

## ABSTRACT
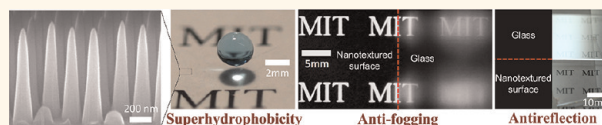


Designing multifunctional surfaces that have user-specified interactions with impacting liquids and with incident light is a topic of both fundamental and practical significance. Taking cues from nature, we use tapered conical nanotextures to fabricate the multifunctional surfaces; the slender conical features result in large topographic roughness, while the axial gradient in the effective refractive index minimizes reflection through adiabatic index-matching between air and the substrate. Precise geometric control of the conical shape and slenderness of the features as well as periodicity at the nanoscale are all keys to optimizing the multifunctionality of the textured surface, but at the same time, these demands pose the toughest fabrication challenges. Here we report a systematic approach to concurrent design of optimal structures in the fluidic and optical domains and a fabrication procedure that achieves the desired aspect ratios and periodicities with few defects and large pattern area. Our fabricated nanostructures demonstrate structural superhydrophilicity or, in combination with a suitable chemical coating, robust superhydrophobicity. Enhanced polarization-independent optical transmission exceeding 98% has also been achieved over a broad range of bandwidth and incident angles. These nanotextured surfaces are also robustly antifogging or self-cleaning, offering potential benefits for applications such as photovoltaic solar cells.

properties. To achieve the high transmissivity required for operation of optical instrumentation under humid conditions in chemical and biological laboratories, antifogging and antireflection as well as enhanced transparency would convey critical advantages, and these multifunctional surface design strategies could also find practical utility in enhanced performance characteristics of common objects such as goggles and
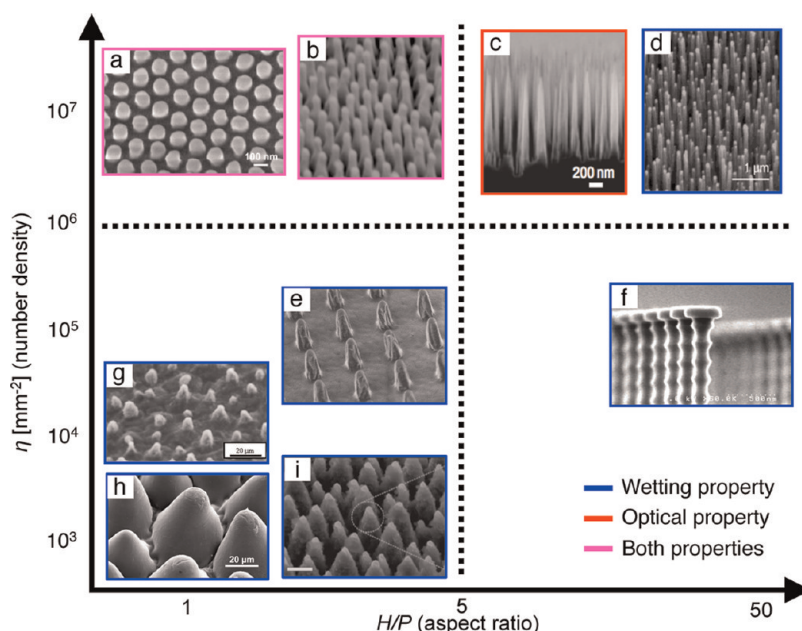
**Figure 1. Plot of the number density ($\eta$) of nanoscale features as a function of the aspect ratio ($H/P$) for natural and artificial surfaces.** The surfaces are (a) mosquito eye, (b) cicada wing, (c) silicon nanostructure, (d) carbon nanotube, (e) perfluoropolyether nanopillar (diameter at the base of pillars ≃500 nm), (f) nanonail, (g) *Calathea zebrina* leaf, (h) lotus leaf, and (i) microconical structure. Panel a reprinted with permission from ref 23. Copyright 2007 Wiley-VCH. Panel b reprinted with permission from ref 18. Copyright 2008 IOP Publishing Ltd. Panel c reprinted with permission from ref 31. Copyright 2007 Nature Publishing Group. Panel d reprinted from ref 12. Copyright 2003 American Chemical Society. Panel f reprinted from ref 13. Copyright 2008 American Chemical Society. Panel g reprinted with permission from ref 1. Copyright 1997 Springer-Verlag. Panel h reprinted with permission from ref 27. Copyright 2009 Elsevier. Panel i reprinted with permission from ref 43. Copyright 2008 Wiley-VCH. To maximize transmission by minimizing reflection, a number density greater than the horizontal borderline (for circumventing interference effects of light) and an aspect ratio close to the vertical borderline (associated with the fracture by bending or buckling of high aspect ratio nanostructure (see Supporting Information)) are required.

vehicle windshields.[22] However, coupled analyses of the functional design constraints followed by integrative design and simultaneous realization of specified wetting and optical functions have been rare and limited to simple pairwise combinations from two distinct fields.[15,19−21,23] The present work is founded on a joint consideration of the wetting and optical physics, starting from analysis and design to implementation using a novel nanolithographic fabrication technique.

## RESULTS AND DISCUSSION

The competing constraints associated with multifunctional features such as water wettability, antireflectivity, optical transparency, and mechanical robustness that we seek in the present work can be compared quantitatively by design charts that rank various natural and artificial surfaces in terms of the number density of features $\eta$, that is, the number of asperities in 1 mm$^2$ (which is inversely proportional to their period $P = 2R$) and their aspect ratio $H/P$, as shown in Figures 1 and 2A. In studies of super-repellency, the canonical natural example is the surface of the lotus leaf, *Nelumbo nucifera* ($\eta \simeq 3 \times 10^3$, $H/P \simeq 0.5$). Studies have revealed that its superhydrophobicity (*i.e.*, exhibiting apparent contact angles with water $\theta^* \geq 150°$ and low contact angle hysteresis) arises from both

hierarchical roughness and the intrinsic chemical characteristics of the surface.

On rough surfaces, the wetting characteristics of water droplets can be explained through two distinct models.[4,5] The Wenzel model[4] describes sessile droplets that fully wet the surface texture. On the other hand, the Cassie−Baxter model[5] describes water droplets that reside partially on the solid texture and partially on a raft of air pockets entrapped within the microscopic texture that enable the surface to become superhydrophobic. On such "Cassie−Baxter surfaces", water droplets can easily roll or bounce off, leading to the ready removal of dust particles and contaminants.[1,10,11] Increasing the aspect ratio ($H/P$) of the texture and incorporating a very low solid-phase surface energy helps to eliminate wetting transitions between the Cassie−Baxter state and the Wenzel state that are associated with contact line depinning events.[10]

In addition to high aspect ratios ($H/P \gg 1$), the feature density, characteristic geometric length scale, and topography of the surface texture all play pivotal roles in creating superhydrophobic surfaces that exhibit robust Cassie−Baxter interfaces and that can resist wetting under dynamic conditions.[11,12,24,25] Studies have shown that an array of high aspect ratio posts with large number density (*e.g.*, a chemically
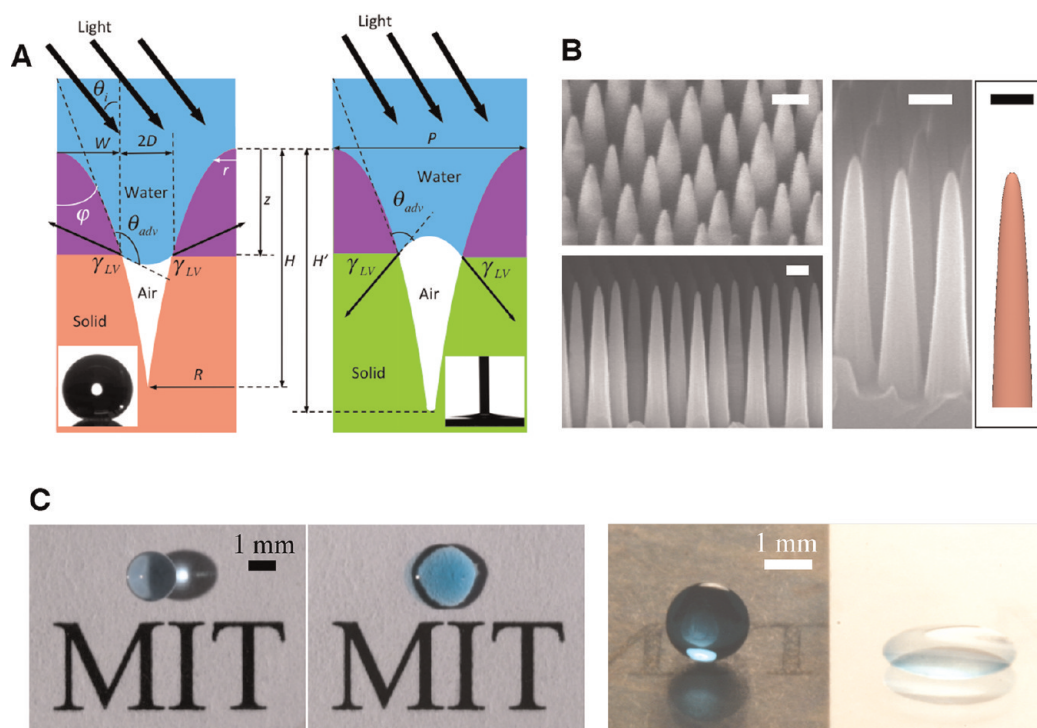
Figure 2. Design and development of optimal nanostructured multifunctional surfaces. (A) Schematic drawings of the three-phase contact line on hydrophobically modified and hydrophilic (as-fabricated) nanotaper structures. The insets show corresponding goniometer images for 5 $\mu$L droplets with apparent contact angles of $\theta^* \simeq 165°$ and $\theta^* \leq 5°$. (B) Micrograph of the final developed nanotaper structure with numerical rendering of a cubic paraboloid. All scale bars represent 200 nm. (C) Blue-dyed water droplets sitting on a transparent nanotaper surface and on flat glass, each placed on top of printed black letters. The two images on the right are oblique views of the same two surfaces. The very weak reflection and high contact angle of the tapered nanocone surface contrast intense reflection and low contact angle of water on flat glass.

treated carbon nanotube forest as shown in Figure 1) can show superhydrophobicity with strong resistance against transition to the Wenzel state.[12,25] This irreversible transition occurs when the applied pressure difference between the liquid drop sitting on the surface and the underlying gas phase (arising, for example, from dynamic external perturbation, such as droplet impact) reaches a critical value.[24] This value is defined as the critical breakthrough pressure $P_{crit}$, that is, the maximum pressure difference that the liquid−air interface can maintain. The key result is that, to achieve greater breakthrough pressure, we require progressively smaller feature spacing.

Moving beyond simple cylindrical post arrays, experiments and calculations on a wide range of surface topographies have suggested that enhanced superhydrophobicity can be obtained by high-density conical or pyramidal structures with small hemispherical caps.[26] Such structures promote a robust Cassie−Baxter state with higher apparent contact angles and lower hysteresis, owing to the very small liquid−solid area fraction $f_s = 2\pi(1 + \cos\theta_{adv})(r/P)^2$ (in the case of an advancing contact angle $\theta_{adv} \geq 90°$ and a square array of conical structures with hemispherical tops) as well as negligible effects of contact line pinning on the hemispherical tops of the features.[26] The conical shape of

the nanotextures developed in the present study also plays an important role in providing greater resistance to loss of superhydrophobicity. The structure is self-stabilizing, and the critical breakthrough pressure increases progressively as the advancing liquid meniscus penetrates into the surface texture due to the continuously decreasing spacing between each cone. This self-stabilization can be quantified by modifying the dimensionless robustness parameter introduced by Tuteja et al.[24] By considering the geometric features in Figure 2A that parametrize the high aspect ratio taper structures, the relevant dimensionless parameter becomes $T^*(z/H) = P_{crit}/P_{ref} = -\pi \ell_{cap}(z/H)^{1/3} \cos(\theta_{adv} - \varphi)/[2P(1 - (\pi/4)(z/H)^{2/3})]$ (see Supporting Information for derivation), where $P_{ref} = 2\gamma_{LV}/\ell_{cap}$ is the reference pressure scale for millimetric drops, $\gamma_{LV}$ is the surface tension, $\ell_{cap} = (\gamma_{LV}/\rho g)^{1/2}$ is the capillary length, $\rho$ is the density of the liquid, $g$ is the gravitational constant, $\theta_{adv}$ is the advancing contact angle of water on a flat chemically homogeneous surface, and $\varphi$ is the cone angle of the feature, as shown in Figure 2A. The magnitude of the critical breakthrough pressure $P_{crit}/P_{ref}$ increases as $z/H \rightarrow 1$ and for smaller values of $P$ (which is proportional to $\eta^{-1}$).

The length scale and shape profile of the conical structure also explain the characteristics of superhydrophilic surfaces such as Calathea zebrina[27] (Figure 1),

which display apparent contact angles with water lower than 10° (shown in the inset of Figure 2A), simply by changing the surface chemistry. By changing the direction of the net surface traction of the three-phase contact line on the hydrophilic conical structure, so that $\theta_{adv} - \varphi < 90°$ (Figure 2A), the liquid meniscus is strongly imbibed into the structure with a traction force that increases as the spacing between features decreases.[28] Higher values of the Wenzel roughness ($r_W$) and of the feature density ($\eta$) in conical nanofeatures can thus also promote superhydrophilicity and progressively smaller apparent contact angles by capillary imbibition.[29] Condensation on such surfaces promotes formation of a continuous liquid film with strong antifogging characteristics.[10,30]

In parallel to these studies of structural control of wetting properties, bioinspired studies on the antireflective optical properties of synthetically fabricated subwavelength structures have been carried out.[31,32] Fresnel reflections occur naturally at all optical interfaces when there is a step discontinuity in refractive index, which can be thought of as an optical impedance mismatch. Structures with subwavelength tapered features, inspired by structures such as those found on the moth eye surface (Figure 1), emulate an effective medium with an axially varying refractive index, which results in adiabatic impedance matching and hence reflection suppression.[15,31] Concomitantly, transmission of incident light through transparent subwavelength conical structures is enhanced over a broad range of wavelengths and incident angles.[32]

By analogy with the robustness measures introduced to rank and compare the resistance to wetting of different nanotexture designs, the transmission enhancing capabilities of a synthetic tapered cone structure can be expressed in terms of dimensionless design parameters that compare the structure height and period with the incident wavelength and angle. Antireflective transparent subwavelength structures behave essentially like a band-pass filter, in which the band-pass range indicates the spectral regime with suppressed Fresnel reflection.[33,34] The upper and lower wavelength bounds ($\lambda_{max}$ and $\lambda_{min}$, respectively) for this band-pass can be tailored by controlling the geometry of the structure and can be approximated as $\lambda_{max} \simeq 2Hn_a \cos\theta_i$ and $\lambda_{min} \simeq P(n_s + n_a \sin\theta_i)$, where $n_s$ and $n_a$ are the refractive indices of the substrate and ambient, respectively, and $\theta_i$ is the incident angle as shown in Figure 2A (see Supporting Information for derivation). Using this analysis, we derive the following expression for the approximate normalized operating bandwidth $B^* = \Delta\lambda/\lambda_{min} = (\lambda_{max} - \lambda_{min})/\lambda_{min} = (H/P)(2n_a \cos\theta_i/(n_s + n_a \sin\theta_i)) - 1$ and use this measure as the nondimensional optical merit function, analogous to the parameter $T^*$ that we used to characterize the wetting behavior. To enhance

transmission bandwidth $B^*$ on nanotextured surfaces, it is again crucial to be able to fabricate subwavelength nanostructures with high aspect ratio ($H/P \gg 1$) and uniformity. This conclusion is entirely consistent with the design requirements we have highlighted for controlling wetting behavior.

As an additional benefit, such tapered cones are more resistant to mechanical instabilities associated with buckling and bending than cylindrical pillars with the same aspect ratio and volume.[35] However, solid mechanical analysis also suggests that very slender structures may lead to structural instabilities under sufficiently large axial or lateral loads. There is thus a trade-off between the fluidic, optical, and structural properties of the texture. The final aspect ratio ($H/P \simeq 5.5$) chosen for the nanotexture fabricated in the present work was selected to be able to withstand the dynamic loads associated with vertical impact of typical raindrops (see Supporting Information).

To simultaneously meet our fluidic and optical design requirements, we fabricated slender tapered cone structures with cone angle $\varphi_{avg} \simeq 4.8°$, on a periodic spacing $P \simeq 200$ nm and height $H = 1.1 \pm 0.05\ \mu m$ with tip radius of curvature $r = 17 \pm 4$ nm directly on a fused silica substrate, as shown in Figure 2B. The aspect ratio $H/P \simeq 5.5$ yields dimensionless design parameter values of $T^* \sim 10^4$ and $B^* \simeq 6.3$ at incident angle $\theta_i = 0°$ (Figure 2A). Our choice of fused silica as the substrate material ensures enhanced transmission at visible and infrared wavelengths; by contrast, previous studies have reported lower bandwidth measures ($1.4 \leq B^* \leq 3.0$) on subwavelength antireflection structures[32,36] or have been based on absorptive materials (e.g., silicon, gallium arsenide, carbon nanotubes, etc.) which suppress surface reflection but do not enhance transmission.[15,31]

The high aspect ratio nanostructures have subwavelength spacing ($P < \lambda$) and were patterned over a large area (>1600 mm²) of the substrate using two orthogonal interference lithography exposures to yield a defect-free periodic square array. Structural superhydrophilicity can be readily attained from the inherent hydrophilicity of the untreated silicon oxide surface. After etching, the structure can be silanized using a standard vapor deposition process to achieve super liquid repellency (see Methods). The final fabricated superhydrophobic and transparent antireflective surface enables a millimetric water droplet (dyed blue in Figure 2C) to form an almost perfect spherical bead (apparent advancing contact angle $\theta_{adv}^* = 165 \pm 1°$, apparent receding contact angle $\theta_{rec}^* = 164 \pm 1°$, and roll-off angle $\theta_{roll-off}^* \leq 2°$).

We represent the relationship between the apparent advancing contact angle $\theta_{adv}^*$ on the nanotextured surface (ordinate) and the advancing contact angle on a flat surface (abscissa) on a wetting diagram

**A**

$\theta_{adv, silanized} = 121.1 \pm 0.5°$    $\theta_{adv, crit} = 95.8°$

Wenzel state

Cassie-Baxter state

$r_W \cong 9.7$

$\theta^*_{adv} = 165.0 \pm 1.0°$

$\cos\theta^*_{adv}$

$\cos\theta_{adv}$

**B**

10 μm    EHT = 30.00 kV    Signal A = CZ BSD    Sample ID =    Peltier Temp = -1.3 °C
Mag = 1.26 K X    WD = 7.5 mm    Chamber = 585 Pa    Humidity = 100.0 %

**C**

Three dimensional
paraboloid model

$\Delta P(z/H)$ [Pa]

Equivalent depth under water [m]

— Paraboloid
— Truncated Cone

$z/H$

**D**

(1) $t = -0.66$ ms    (2) $t = 0.14$ ms    (3) $t = 0.93$ ms
5 mm

(4) $t = 4.61$ ms    (5) $t = 8.29$ ms    (6) $t = 12.0$ ms

(7) $t = 15.7$ ms    (8) $t = 19.3$ ms    (9) $t = 23.0$ ms
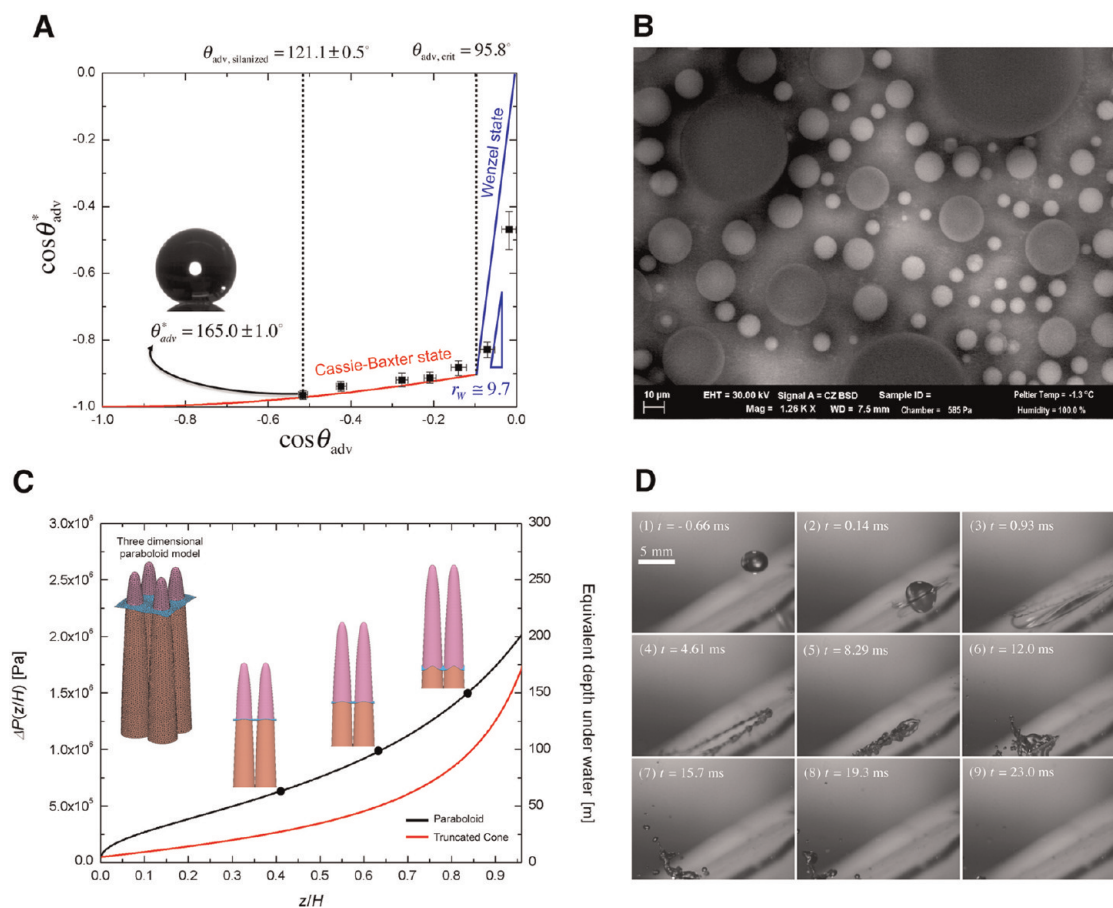
**Figure 3.** Extreme wetting properties of the nanocone structure. (A) Wetting diagram with experimental results obtained using droplets of water−ethanol mixtures with various compositions sitting on silane-treated flat ($\theta^*$) and tapered nanocone ($\theta_{adv}^*$) surfaces. The inset represents a pure water droplet sitting on the silanized nanotaper surface (bottom left). (B) Environmental scanning electron microscope image of condensing water drops on the silanized nanocone surface showing spherical droplets resting on the tips of the nanotaper surface. (C) Calculation of the pressure difference $\Delta P(z/H)$ that the water−air interface can resist at given penetration depths into the structure, based on the simple analytic scaling of the dimensionless robustness parameter ($T^*$). (D) Sequential images of a water droplet impact on an oblique (30° from the horizontal plane) nanotaper surface (taken through the use of a high-speed camera; $V_{imp} \simeq 6.26$ m/s and $We \simeq 1785$). The last image on the bottom right side shows that no residual droplets remain on the nanotaper surface due to the high robustness of the Cassie−Baxter state to the dynamic pressure.

(see Figure 3A).[37] The red and blue lines indicate the thermodynamically stable Wenzel state or Cassie−Baxter state, respectively.[37] The crossover point at $\theta_{crit}$ can be calculated by equating the energies for the two distinct wetting states.[10,28] Advancing contact angles above this value lead to a lower overall free energy for droplets in the Cassie−Baxter state as compared to the corresponding Wenzel state.[28] Contact angle measurements using a range of water−ethanol mixtures possessing different surface tensions (47.2 mN/m $\leq \gamma_{LV} \leq$ 72.0 mN/m) and different advancing contact angles $\theta_{adv}$ on flat silanized silica glass wafers confirm the predictions of the two models for the evolution in the apparent advancing contact angle observed on the silanized nanotextured surface.

To quantify the robustness of the macroscopic non-wetting behavior of these surfaces, we investigate nucleation and condensation phenomena *in situ* using an environmental scanning electron microscope

(ESEM, Zeiss Evo 55). The micrograph in Figure 3B demonstrates that the nanotexture supports a nonwetting Cassie−Baxter state with microscopic spherical droplets. The maximum sustainable pressure difference for this surface can be estimated to be $\Delta P = 2\gamma_{LV}/r_d \simeq 96$ kPa, where $r_d \simeq 1.5$ μm is the radius of the smallest droplet observable.

In addition to quantifying the capillary hydrostatics of droplets at rest on the nanotextured surface, the hydrodynamic interactions of impacting rain droplets with textured solid surfaces is an important design feature of robust superhydrophobic surfaces deployed in the environment. The weak shock generated by the impact of a droplet on a rigid impenetrable surface can generate dynamic pressures that are much higher than the static Laplace pressure.[38] The initial impact generates a water hammer pressure ($P_{WH} \sim 0.5\rho c V$) where $\rho$ is the density of water, $c$ is speed of sound in water, and $V$ is impact velocity, which decays rapidly to a

Bernoulli pressure ($P_B \sim \rho V^2$).[39−41] Under these dynamic conditions, even apparently robust textured nonwetting surfaces can lose their superhydrophobicity.[42] For example, while typical micrometric textured post arrays can support breakthrough pressure on the order of 1 kPa,[11] the maximum dynamic impact pressure of raindrops with typical impact velocities in the range of 0.3 m/s $\leq V \leq$ 5 m/s[43] is approximately 1000 times higher, corresponding to pressure differences in the range of 0.23 MPa $\leq P_{WH} \leq$ 3.8 MPa. As a result of the progressively decreasing spacing between neighboring high aspect ratio asperities, the high-density tapered conical structure exhibits extremely high breakthrough pressures corresponding to several MPa, as shown in Figure 3C. Evaluation of our modified design parameter $T^*$ provides a simple analytic expression for the maximum pressure (assuming the liquid meniscus between four asperities forms a hemispherical liquid cap) $P_{crit} = T^*(z/H \rightarrow 1) \times P_{ref} \simeq 2.3$ MPa. This estimate is supported by more complete numerical calculations using Surface Evolver[44] (see Supporting Information) which show that the critical breakthrough pressure monotonically increases as the three-phase contact line advances into the valleys between the tapered cone. These exceedingly high values of critical breakthrough pressure and the concomitant self-stabilization effect stem from the tapered conical structure, which results in the minimum spacing on the order of tens of nanometers near the bottom of each valley. The sequence of high-speed camera (Vision Research Phantom v5.0) images shown in Figure 3D following impact of a water drop ($V \simeq$ 6.26 m/s, corresponding to Weber number $We \simeq$ 1758) clearly shows the consequences of this self-stabilization effect, with complete droplet rebound and roll-off at higher impact velocities than previous dynamic studies.[11,42,43]

The slender tapered nanocone structures also exhibit enhanced optical transmissivity. In Figure 4A,B, we show the measured transmission for a flat fused silica surface and for single-sided and double-sided nanotexture surfaces. The measurements were carried out over a wide range of incident angles from 0 to 80° using both TE-polarized and TM-polarized irradiation with a wavelength $\lambda$ = 632.8 nm, and the measured transmission data agree well with theoretical calculations by rigorous coupled wave analysis (see Supporting Information).

As shown in Figure 4A, the measured transmission of TE-polarized light through the double-sided nanotextured surface was enhanced to be above 90% even for incident angles as large as 75° thanks to the high aspect ratio and slow taper; by contrast, the transmission of flat glass drops to 38%. For the single-sided nanocone surface, the transmission is limited by Fresnel reflection arising from the step discontinuity in the refractive index at the flat rear surface.

The measured transmission values of TM-polarized light through the single- and double-sided nanotaper surfaces are greater than 90% at 70°, as shown in Figure 4B. The double-sided nanotextured surface has slightly lower measured transmission than the single-sided surfaces from 40 to 70° due to the accumulation of defects induced during the sequential fabrication of nanocone arrays on both sides of the substrate, and the transmission shows no Brewster peak since there is no step discontinuity in the refractive index.[45] The single-sided surface, on the other hand, still exhibits the Brewster effect on the rear surface, and the transmission increases up to 99.4% at 56°.

The transmission measurements through the double-sided surfaces were also carried out over a broad range of wavelengths (250 nm $\leq \lambda \leq$ 1700 nm) using TE-polarized and TM-polarized irradiation at incident angles $\theta_i$ = 0, 30, 45, and 60°. In Figure 4C,D, the double-sided surface exhibits transmission greater than 98% at $\theta_i$ = 0° over a wide range of wavelengths. The measurements show a decrease in transmission ($\theta_i$ = 0°) at a lower wavelength bound of approximately 300 nm because the 200 nm period nanocone structure becomes increasingly diffractive. The transmission measurements at incident angles $\theta_i$ = 30, 45, and 60° demonstrate that the minimum wavelength bound ($\lambda_{min}$) increases with increasing incident angle for both polarized lights, which typically narrows the operational bandwidth for omnidirectional transmission (see Supporting Information). Figure 4E shows the arithmetically averaged transmission of the experimental results shown in Figure 4C (TE-polarized light) and D (TM-polarized light).

To quantify the effectiveness of the nanocone surface for possible application as an outer protective layer for photovoltaic cells, we define a spectrally averaged transmittance $S(\theta_i) = \int_{\lambda_a}^{\lambda_b} Sr(\lambda) \times T(\lambda,\theta_i)d\lambda / \int_{\lambda_a}^{\lambda_b} Sr(\lambda)d\lambda$, which yields the power collection efficiency if multiplied by the quantum efficiency. Here $Sr(\lambda)$ is the spectral solar irradiance at sea level[46] and $T(\lambda,\theta_i)$ is the arithmetically averaged transmission of the surfaces as a function of wavelength and incident angle. For the tapered nanocones fabricated here, the spectrally averaged transmittance $S(\theta_i = 0, 30, 45, 60°)$ from $\lambda_a$ = 300 nm to $\lambda_b$ = 1100 nm are 0.98, 0.97, 0.95, and 0.94, respectively. The invariance of these values shows that the irradiation transmitted to a solar cell covered with such a surface texture will not vary with the solar elevation angle. By contrast, a flat fused silica surface yields values $S(\theta_i = 0, 30, 45, 60°$ and from $\lambda_a$ = 300 nm to $\lambda_b$ = 1100 nm) = 0.93, 0.92, 0.91, and 0.85.

In many practical applications, including solar panels, self-cleaning and prevention of contaminant fouling or avoidance of fogging are also important to preserve high transmission. These deterrents are largely mitigated in our nanotextured surfaces again due,
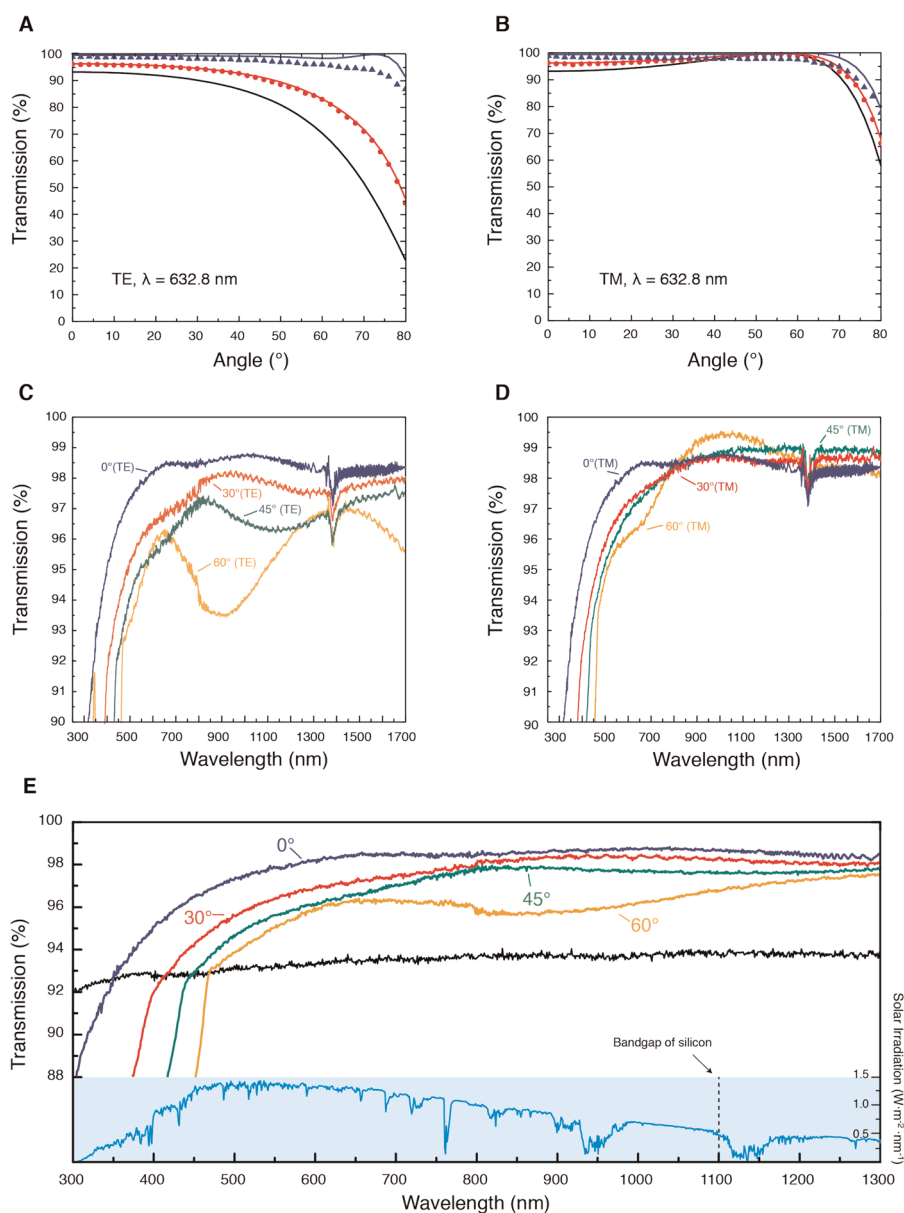
**Figure 4.** Enhanced broadband, omnidirectional optical transmission of the nanotaper structure. (A,B) Optical transmission for both transverse electric (TE) and transverse magnetic (TM) polarized light through the single- and double-sided nanotaper surfaces (represented in red circle and blue triangle, respectively) is measured by changing the incident angle of a laser source. The theoretical model results calculated by using rigorous coupled wave analysis are also shown in solid lines (flat fused silica surface in black, single-sided nanotaper surface in red, and double-sided nanotaper surface in blue) for comparison. (C,D) Measured broadband transmission for TE-polarized and TM-polarized lights at the four different incident angles with a wide range of wavelength. (E) Averaged broadband transmission with two measurements on both TE and TM polarizations in C and D at the four different incident angles with a range of wavelengths (300 nm $\leq \lambda \leq$ 1300 nm). The black line is the measured broadband transmission of the flat fused silica surface at normal incident angle. Spectral solar irradiation data (light blue) with respect to the same wavelength are shown in the inset for reference, and the dashed black line depicts the band gap of crystalline silicon, one of materials used for solar cells, which means that no light can be absorbed in photovoltaic devices for wavelengths greater than this value.

respectively, to either superhydrophobicity or structural superhydrophilicity. To quantify, we compared changes in the transmission of the nanotextured surface and a flat silica surface after contaminant fouling using a 632.8 nm red laser at normal incidence. The transmission tests in Figure 5A,B show that for three different common particulate contaminants placed on the nanotextured surfaces the surfaces can be

completely cleaned by at most three droplet impacts, whereas water droplets are ineffective at cleaning the conventional flat glass surfaces due to the hysteretic pinning of residual water droplets.

As shown in Figure 5C, a clear in-focus image of the white letters transmitted through the untreated nanotextured surface also demonstrates qualitatively the antifogging property conferred by structural superhydrophilicity.
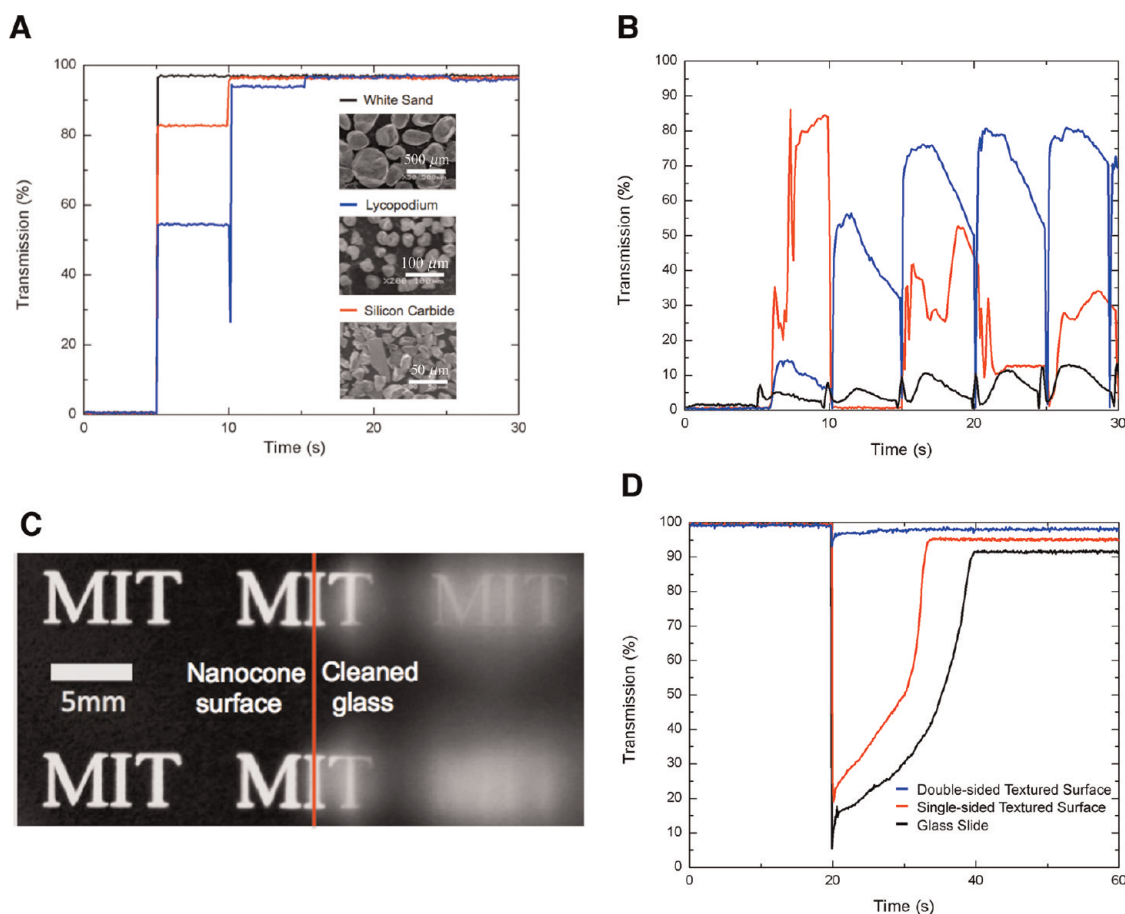
**Figure 5.** Optical transmission measurements for quantifying the self-cleaning and antifogging properties of the nanocone surfaces. (A,B) Evolution of the transmission of 632.8 nm red laser through surface-contaminated tapered nanocone surface and flat glass surfaces, respectively. The transmission measurements were recorded while water droplets were released from a height of 10 mm (corresponding to impact velocity $V \simeq 0.44$ m/s, $We = 6.9$) from the inclined surfaces (30°) every 5 s. The apparent contact angles ($\theta^* > 160°$) as well as contact angle hysteresis (CAH < 3°) of our superhydrophobic nanotextured surface remained unaltered after more than 100 realizations of the self-cleaning tests that were carried out over a period of greater than 6 months.[53] (C) Image of printed letters viewed through fogged (nanocone (left) and flat glass (right)) surfaces. (D) Change of transmission due to fogging and defogging on double-sided nanotaper (blue), single-sided nanotaper (red), and flat cleaned glass (black) surfaces.

When viewed through a conventional hydrophilic flat glass surface placed adjacently, the image is much more blurry by comparison. We quantify this difference in Figure 5D by measuring the time evolution of transmissivity after exposing the nanotextured and conventional surfaces to a stream of saturated steam and then placing the surfaces (at $t = 5$ s) into the path of the laser beam. Transmission through the fogged flat glass slide rapidly drops and then gradually increases to a constant value that remains lower than that of the tapered cone surface. This loss of transmissivity on the flat hydrophilic surface is due to the deposition of microscopic droplets that remain pinned on the surface, as well as intrinsic reflection on the glass slide.[47] On the other hand, measurements on the double-sided nanotextured surface shows an immediate recovery of transmission to a very high plateau value as a result of rapid imbibition of the thin layer of water followed by a uniform evaporation rate across the entire surface.

## CONCLUSION

By developing a novel double mask etching process for large-area patterning on silicon oxide substrates, we have demonstrated that subwavelength tapered conical structures with high aspect ratio and large packing densities result in multifunctional surfaces with enhanced liquid wettability and omnidirectional transparency across a broad spectrum of visible and near-infrared wavelengths. By combining observations of various natural textured surfaces and quantitative analysis of the underlying physical principles controlling wetting, optical transmission, and mechanical robustness, the dimension and slenderness of the nanocone structures have been optimized to achieve superior antiwetting performance and optical transmissivity. Texturing square arrays of these tapered nanocones on both sides of a flat silicon oxide substrate, followed by a suitable chemical modification of the solid surface energy, enables us to show that it is
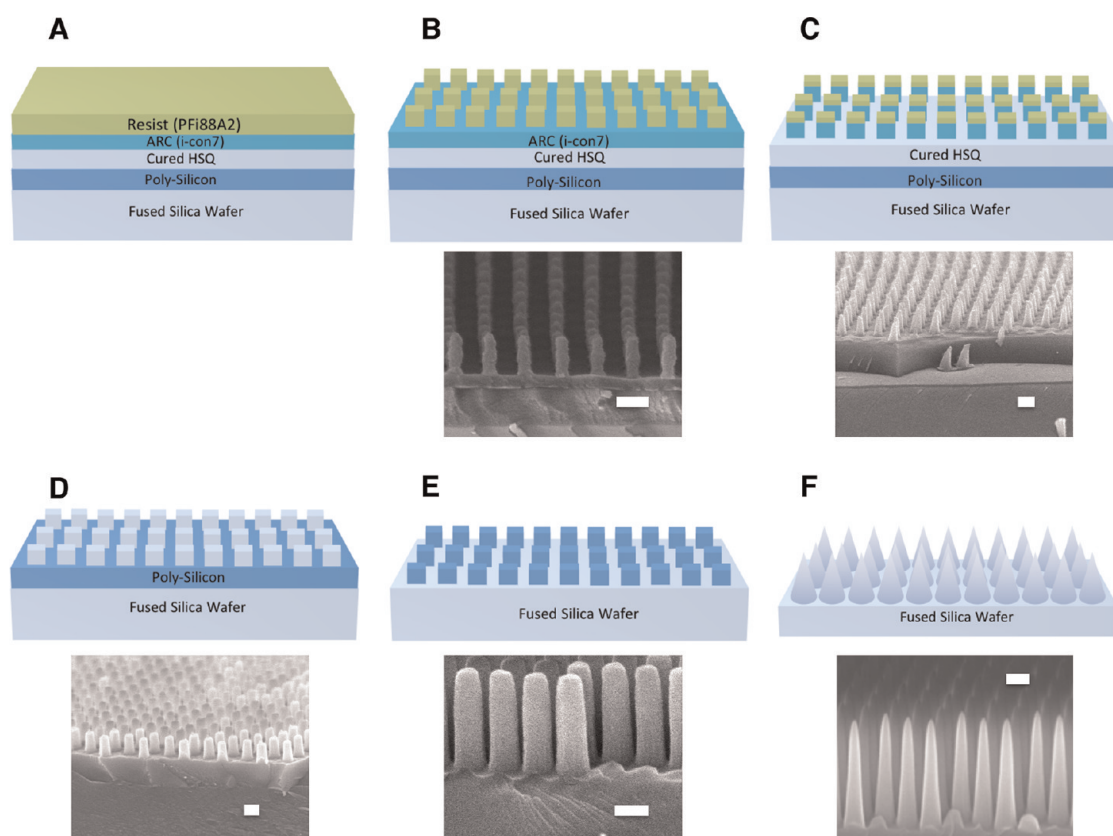
**Figure 6. Stages of the fabrication process. (A) Deposition of multiple coating layers. (B) Development of photoresist pattern. (C−F) Subsequent etching steps of antireflective coating layer (C), cured HSQ layer (D), polysilicon layer (E), and fused silica wafer (F). All of the white scale bars on the micrographs represent 200 nm.**

possible to combine robust superhydrophobicity (or superhydrophilicity) with minimal scattering or reflection of light over a wide range of incident angles, wavelengths and polarization states. Additional optical transmission experiments have demonstrated and quantified the macroscopic self-cleaning and antifogging functionalities of the nanocone structures, suggesting numerous practical engineering applications including photovoltaic cells, windshields, and goggles. Nanotextured surfaces of the type discussed in the present paper can be produced in larger scale; scanning beam interference lithography tools and large chamber plasma etchers have been employed to fabricate nanostructures over surfaces as large as 12 in. wafers.[48] Alternative methods for large-scale, low-cost, high-throughput manufacturing of functional nanostructures have also been described, including replication into bulk metallic glass[49] or through the use of roll-to-roll nanoimprinting technology with ultraviolet-curable polymers.[50]

## METHODS

**Fabrication of Tapered Nanocone Surfaces.** For the fabrication of nanotextured surfaces, each of the thicknesses of the multiple coated layers on a 6 in. ultraviolet (UV) grade double-side-polished fused silica wafer (thickness = 550 $\mu$m) was optimized for interference lithography[51,52] (Figure 6A). Polysilicon films (300 nm) were deposited on both sides of the fused silica wafer with a chemical vapor deposition technique for realizing a high aspect ratio silicon oxide structures. Photoresist (S1813, Shipley, 4 $\mu$m) was spun onto both sides of the polysilicon layers of the fused silica wafer as a protective layer, and the wafer was cut into 4 samples (45 mm × 45 mm). The photoresist on the top of the polysilicon was cleaned with *N*-methylpyrrolidone (NMP, positive resist stripper, BASF) and RCA cleaning for 20 min and was sonicated for 5 min at room temperature. Hydrogen silsequioxane (HSQ14, Dow Corning, 340 nm) films were then spun on both sides of the sample and hard-baked at 500 °C in

the oven for 11 h to be cured as the first hardmask because a cured HSQ layer is similar to a SiO$_2$ etch mask layer.

After RCA cleaning, sonication, and plasma oxygen etching for 30 s in order to remove organic particulates, an antireflective coating layer (I-con 7, Brewer Science, 105 nm) was spun on the both sides and baked at 180 °C in the oven for 1 h. For baking, an oven was used instead of a hot plate because both sides of the sample need to be protected equally. A positive photoresist (PFi-88A2, Sumitomo, 250 nm) was spun on only one side of the sample, while the photoresist (S1813, Shipley, 4 $\mu$m) was spun on the backside of the sample as a protective layer. This was then baked on the hot plate at 90 °C for 90 s. Using Lloyd's mirror, a $\lambda$ = 325 nm wavelength laser beam makes an interference pattern with a 200 nm period standing wave projected onto the photoresist. Two separate orthogonal laser exposures (each expose dose = 21.35 mJ/cm$^2$) were projected onto the photoresist at the incident angle of 54.34° for 5 min each, with an interval time of 1 min (to avoid burning of the photoresist),

and the exposed photoresist is developed to leave a pattern of posts (Figure 6B).

Oxygen and $CHF_3$ reactive ion etching processes were used to remove the residual photoresist and open the polysilicon surface from cured HSQ. We kept the pressure at 7 mTorr and a microwave power level of 100 W and used 20 sccm of oxygen plasma etching for 45 s (Figure 6C) to etch the antireflective coating layer. Then we used 20 sccm of $CHF_3$ at a voltage of 350 V and the pressure at 10 mTorr with the power ranging between 100 and 170 W during the etch for 14 min in order to etch the cured HSQ layer (Figure 6D). The cured HSQ pattern was transferred without defect to the polysilicon layer (300 nm) with HBr reactive ion etching. For etching the polysilicon layer, we used 20 sccm of HBr for 6 min, keeping the pressure at 10 mTorr and a microwave power level of 200 W during the process. Finally, a voltage of 350 V and a pressure of 10 mTorr were retained while we used 20 sccm of $CHF_3$ with the power ranging between 100 and 220 W during the final process for 40 min to etch the fused silica wafer (Figure 6E). The different etch rates between the hard masks and fused silica enable realization of the high aspect ratios (Figure 6F).

To obtain better optical performance, the fused silica must be patterned on both sides. Additional repeatable processes were conducted as described below. After 40 min of RCA cleaning, the photoresist (S1813, 4 $\mu$m) was spun onto the patterned surface being shielded. An antireflective coating material and positive photoresist (PFi-88) were spun onto the backside of the sample, consecutively. A pattern of photoresist posts was again fabricated with double exposures and subsequent development, and this was transferred down to fused silica with the same fabrication steps and conditions described above. After RCA cleaning, the rest of the polysilicon layers was removed by tetramethylammonium hydroxide (TMAH) etching (25 wt %) for 1 min at 80 °C without influencing the fabricated fused silica nanostructures on both sides. To change the surface hydrophobic, the surface was then treated by a chemical vapor deposition of 1$H$,1$H$,2$H$,2$H$-perfluorodecyltrichlorosilane[53] (Alfa Aesar, 96%) in an oven at 110 °C for 10 h.

**Contact Angle Measurements.** Advancing and receding contact angle measurements were performed using a Ramé-Hart model 590 goniometer, by dispensing liquid droplets of volume $V \simeq 5$ $\mu$L and adding volume to the droplets at the flow rate of 10 $\mu$L/s. Roll-off angles were measured by using an automatic tilting stage at a rate of 1°/s.

**Optical Transmission Measurements.** Optical transmission measurements were carried out using two optical measurement systems. A Cary-500 (UV–vis–NIR) spectrophotometer was used for the polarization-dependent transmission measurements in the UV–vis–NIR range (250–1700 nm) with a Glan-Taylor polarizer (PGT-S1 V). A stabilized helium–neon laser (632.8 nm) was used to measure the transmission incident angle with a 20LP-VIS-B Precision linear polarizer. The angular resolution of the instruments was 0.07°.

*Conflict of Interest:* The authors declare no competing financial interest.

*Supporting Information Available:* Additional information on critical stresses leading to fracture by bending or buckling of slender nanotexture, dimensionless measure of robustness $T^*(z/H)$ of the Cassie–Baxter state against an applied pressure difference across the water–air interfaces, a computational model to calculate the meniscus location of water–air interfaces contacting the nanotaper structures under various imposed pressure differences, dimensionless measure of optical transmission bandwidth for the characterization of antireflective tapered nanocone surfaces, and measurements of broadband and omnidirectional optical transmission of the double-sided nanotaper surfaces. This material is available free of charge *via* the Internet at http://pubs.acs.org.

*Note Added after ASAP Publication:* After this paper was published online May 1, 2012, a correction was made to Figure 2. The corrected version was reposted May 10, 2012.

## REFERENCES AND NOTES

1. Barthlott, W.; Neinhuis, C. Purity of the Sacred Lotus, or Escape from Contamination in Biological Surfaces. *Planta* **1997**, *202*, 1–8.
2. Clapham, P. B.; Hutley, M. C. Reduction of Lens Reflection by Moth Eye Principle. *Nature* **1973**, *244*, 281–282.
3. Hamilton, W. J.; Seely, M. K. Fog Basking by the Namib Desert Beetle, *Onymacris unguicularis*. *Nature* **1976**, *262*, 284–285.
4. Wenzel, R. N. Resistance of Solid Surfaces to Wetting by Water. *Ind. Eng. Chem.* **1936**, *28*, 988–994.
5. Cassie, A. B. D.; Baxter, S. Wettability of Porous Surfaces. *Trans. Faraday Soc.* **1944**, *40*, 0546–0550.
6. Parker, A. R.; Lawrence, C. R. Water Capture by a Desert Beetle. *Nature* **2001**, *414*, 33–34.
7. Wilson, S. J.; Hutley, M. C. The Optical Properties of "Moth Eye" Antireflection Surfaces. *Opt. Acta* **1982**, *29*, 993–1009.
8. Parker, A. R.; Townley, H. E. Biomimetics of Photonic Nanostructures. *Nat. Nanotechnol.* **2007**, *2*, 347–353.
9. Lafuma, A.; Quéré, D. Superhydrophobic States. *Nat. Mater.* **2003**, *2*, 457–460.
10. Quéré, D. Wetting and Roughness. *Annu. Rev. Mater. Res.* **2008**, *38*, 71–99.
11. Bhushan, B.; Jung, Y. C.; Koch, K. Micro-, Nano- and Hierarchical Structures for Superhydrophobicity, Self Cleaning, and Low Adhesion. *Philos. Trans. R. Soc., A* **2009**, *367*, 1631–1672.
12. Lau, K. K. S.; Bico, J.; Teo, K. B. K.; Chhowalla, M.; Amaratunga, G. A. J.; Milne, W. I.; McKinley, G. H.; Gleason, K. K. Superhydrophobic Carbon Nanotube Forests. *Nano Lett.* **2003**, *3*, 1701–1705.
13. Ahuja, A.; Taylor, J. A.; Lifton, V.; Sidorenko, A. A.; Salamon, T. R.; Lobaton, E. J.; Kolodner, P.; Krupenkin, T. N. Nanonails: A Simple Geometrical Approach to Electrically Tunable Superlyophobic Surfaces. *Langmuir* **2008**, *24*, 9–14.
14. Bernard, C. G. Structural and Functional Adaptation in a Visual System. *Endeavour* **1967**, *26*, 79–84.
15. Kanamori, Y.; Sasaki, M.; Hane, K. Broadband Antireflection Gratings Fabricated upon Silicon Substrates. *Opt. Lett.* **1999**, *24*, 1422–1424.
16. Lalanne, P.; Morris, G. M. Antireflection Behavior of Silicon Subwavelength Periodic Structures for Visible Light. *Nanotechnology* **1997**, *8*, 53–56.
17. Barnes, G. A.; Flaim, T. D.; Jones, S. F.; Bruce, J.; Dudley, W.; Koester, D. A.; Peters, C. R.; Bobbio, S. M. Antireflective Coating for Deep UV Lithography Process Enhancement. *Polym. Eng. Sci.* **1992**, *32*, 1578–1582.
18. Xie, G.; Zhang, G.; Lin, F.; Zhang, J.; Liu, Z.; Mu, S. The Fabrication of Subwavelength Anti-reflective Nanostructures Using a Bio-template. *Nanotechnology* **2008**, *19*, 095605.
19. Xia, F.; Jiang, L. Bio-inspired, Smart, Multiscale Interfacial Materials. *Adv. Mater.* **2008**, *20*, 2842–2858.
20. Min, W.-L.; Jiang, B.; Jiang, P. Bioinspired Self-Cleaning Antireflection Coatings. *Adv. Mater.* **2008**, *20*, 3914–3918.
21. Zhu, J.; Hsu, C. M.; Yu, Z. F.; Fan, S. H.; Cui, Y. Nanodome Solar Cells with Efficient Light Management and Self-Cleaning. *Nano Lett.* **2010**, *10*, 1979–1984.

22. Lee, H. J.; Willis, C. Dressed for Combat. *Chem. Ind.* **2009**, 21–23.

23. Gao, X.; Yan, X.; Yao, X.; Xu, L.; Zhang, K.; Zhang, J.; Yang, B.; Jiang, L. The Dry-Style Antifogging Properties of Mosquito Compound Eyes and Artificial Analogues Prepared by Soft Lithography. *Adv. Mater.* **2007**, *19*, 2213–2217.

24. Tuteja, A.; Choi, W.; Mabry, J. M.; McKinley, G. H.; Cohen, R. E. Robust Omniphobic Surfaces. *Proc. Natl. Acad. Sci. U.S.A.* **2008**, *105*, 18200–18205.

25. Journet, C.; Moulinet, S.; Ybert, C.; Purcell, S. T.; Bocquet, L. Contact Angle Measurements on Superhydrophobic Carbon Nanotube Forests: Effect of Fluid Pressure. *Europhys. Lett.* **2005**, *71*, 104–109.

26. Nosonovsky, M.; Bhushan, B. Roughness Optimization for Biomimetic Superhydrophobic Surfaces. *Microsyst. Technol.* **2005**, *11*, 535–549.

27. Schulte, A. J.; Koch, K.; Spaeth, M.; Barthlott, W. Biomimetic Replicas: Transfer of Complex Architectures with Different Optical Properties from Plant Surfaces on Technical Materials. *Acta Biomater.* **2009**, *5*, 1848–1854.

28. Tuteja, A.; Choi, W.; McKinley, G. H.; Cohen, R. E.; Rubner, M. F. Design Parameters for Superhydrophobicity and Superoleophobicity. *MRS Bull.* **2008**, *33*, 752–758.

29. Reyssat, M.; Courbin, L.; Reyssat, E.; Stone, H. A. Imbibition in Geometries with Axial Variations. *J. Fluid Mech.* **2008**, *615*, 335–344.

30. Cebeci, F. C.; Wu, Z. Z.; Zhai, L.; Cohen, R. E.; Rubner, M. F. Nanoporosity-Driven Superhydrophilicity: A Means To Create Multifunctional Antifogging Coatings. *Langmuir* **2006**, *22*, 2856–2862.

31. Huang, Y.-F.; Chattopadhyay, S.; Jen, Y.-J.; Peng, C.-Y.; Liu, T.-A.; Hsu, Y.-K.; Pan, C.-L.; Lo, H.-C.; Hsu, C.-H.; Chang, Y.-H.; et al. Improved Broadband and Quasi-omnidirectional Anti-reflection Properties with Biomimetic Silicon Nanostructures. *Nat. Nanotechnol.* **2007**, *2*, 770–774.

32. Choi, K.; Park, S. H.; Song, Y. M.; Lee, Y. T.; Hwangbo, C. K.; Yang, H.; Lee, H. S. Nano-Tailoring the Surface Structure for the Monolithic High-Performance Antireflection Polymer Film. *Adv. Mater.* **2010**, *22*, 3713–3718.

33. Deinega, A.; Valuev, I.; Potapkin, B.; Lozovik, Y. Minimizing Light Reflection from Dielectric Textured Surfaces. *J. Opt. Soc. Am. A* **2011**, *28*, 770–777.

34. Grann, E. B.; Moharam, M. G.; Pommet, D. A. Optimal Design for Antireflection Tapered Two Dimensional Subwavelength Grating Structure. *J. Opt. Soc. Am. A* **1995**, *12*, 333–339.

35. Timoshenko, S. P.; Gere, J. M. *Theory of Elastic Stability*; McGraw-Hill: New York, 1961.

36. Li, Y.; Zhang, J.; Zhu, S.; Dong, H.; Jia, F.; Wang, Z.; Tang, Y.; Zhang, L.; Zhang, S.; Yang, B. Bioinspired Silica Surfaces with Near-Infrared Improved Transmittance and Superhydrophobicity by Colloidal Lithography. *Langmuir* **2010**, *26*, 9842–9847.

37. Onda, T.; Shibuichi, S.; Satoh, N.; Tsujii, K. Super-Water-Repellent Fractal Surfaces. *Langmuir* **1996**, *12*, 2125–2127.

38. Eggers, J.; Fontelos, M. A.; Josserand, C.; Zalesk, S. Drop Dynamics after Impact on a Solid Wall: Theory and Simulations. *Phys. Fluids* **2010**, *22*, 062101.

39. Lesser, M. Analytic Solutions of Liquid-Drop Impact Problems. *Proc. R. Soc. A* **1981**, *377*, 289–308.

40. Rosenblatt, M.; Ito, Y. M.; Eggum, G. E. Analysis of Brittle Target Fracture from a Subsonic Water Drop Impact. In *Erosion: Prevention and Useful Applications*; Adler, W. F., Ed.; American Society for Testing and Materials: Philadelphia, PA, 1979; pp 227–254.

41. Sanada, T.; Ando, K.; Colonius, T. In *Numerical Analysis of High Speed Droplet Impact*, 7th Intl. Conf. on Multiphase Flow, Tampa, FL, May 30–June 4, **2010**.

42. Li, X.; Ma, X.; Lan, Z. Dynamic Behavior of the Water Droplet Impact on a Textured Hydrophobic/Superhydrophobic Surface: The Effect of the Remaining Liquid Film Arising on the Pillars' Tops on the Contact Time. *Langmuir* **2009**, *26*, 4831–4838.

43. Zorba, V.; Stratakis, E.; Barberoglou, M.; Spanakis, E.; Panagiotis, T.; Anastasiadis, S. H.; Fotakis, C. Biomimetic Artificial Surfaces Quantitatively Reproduce the Water Repellency of a Lotus Leaf. *Adv. Mater.* **2008**, *20*, 4049–4054.

44. Brakke, K. A. The Surface Evolver. *Exp. Math.* **1992**, *1*, 141–165.

45. Chuang, S.-Y.; Chen, H.-L.; Shieh, J.; Lin, C.-H.; Cheng, C.-C.; Liu, H.-W.; Yu, C.-C. Nanoscale of Biomimetic Moth Eye Structures Exhibiting Inverse Polarization Phenomena at the Brewster Angle. *Nanoscale* **2010**, *2*, 799–805.

46. *Standard Terrestrial Direct Normal Solar Spectral Irradiance Tables for Air Mass 1.5*; American Society for Testing of Materials: Philadelphia, PA, 1982.

47. Srinivasarao, M.; Collings, D.; Philips, A.; Patel, S. Three-Dimensionally Ordered Array of Air Bubbles in a Polymer Film. *Science* **2001**, *292*, 79–83.

48. Heilmann, R.; Chen, C.; Konkola, P.; Schattenburg, M. Dimensional Metrology for Nanometre-Scale Science and Engineering: Towards Sub-nanometre Accurate Encoders. *Nanotechnology* **2004**, *15*, S504–S511.

49. Schroers, J. Processing of Bulk Metallic Glass. *Adv. Mater.* **2009**, *22*, 1566–1597.

50. Kim, J.-G.; Sim, Y.; Cho, Y; Seo, J.-W.; Kwon, S.; Park, J.-W.; Choi, H.; Kim, H.; Lee, S. Large Area Pattern Replication by Nanoimprint Lithography for LCD-TFT Application. *Microelectron. Eng.* **2009**, *86*, 2427–2431.

51. Fujita, S.; Maruno, S.; Watanabe, H.; Kusumi, Y.; Ichikawa, M. Periodical Nanostructure Fabrication Using Electron Interference Fringes Produced by Scanning Interference Electron Microscope. *Appl. Phys. Lett.* **1995**, *66*, 2754–2756.

52. Lasagni, A.; Seyler, M.; Holzapfel, C.; Maier, W.; Mücklich, F. Periodical Gratings in Mixed Oxide Films by Laser Interference Irradiation. *Adv. Mater.* **2005**, *17*, 2228–2232.

53. Kobrin, B.; Zhang, T.; Grimes, M. T.; Chong, K.; Wanebo, M.; Chinn, J.; Nowak, R. An Improved Chemical Resistance and Mechanical Durability of Hydrophobic FDTS Coatings. *J. Phys.: Conf. Ser.* **2006**, *34*, 454–457.